International Journal of Plasticity 100 (2018) 52–68

Contents lists available at ScienceDirect

International Journal of Plasticity

journal homepage: www.elsevier.com/locate/ijplas

Microstructural and micromechanical evolution during dynamic recrystallization

Pengyang Zhao [a, *], Yunzhi Wang [a], Stephen R. Niezgoda [a, b]

[a] Department of Materials Science and Engineering, The Ohio State University, United States
[b] Department of Mechanical and Aerospace Engineering, The Ohio State University, United States

ARTICLE INFO

Article history:
Received 31 July 2017
Accepted 15 September 2017
Available online 20 September 2017

Keywords:
Dynamic recrystallization
Thermomechanical processes
Crystal plasticity
Phase-field
Microstructures

ABSTRACT

Dynamic recrystallization (DRX) can in principle serve as an alternative way of controlling grain structure via a single route of hot working instead of the traditional cold working followed by annealing at elevated temperatures; in reality, its widespread application is hindered by the lack of quantitative understanding and prediction of the process. Using a recently developed model (Zhao et al., 2016) that integrates a fast Fourier transform-based elasto-viscoplastic model and a phase-field recrystallization model, we investigate the evolution of both microstructural and micromechanical fields in polycrystal copper during uniaxial compression at various elevated temperatures. Quantitative analysis based on the simulation results confirms that stress redistribution upon the formation of a new grain can significantly lower the dislocation density of neighboring grains, leading the so-called "DRX-enhanced recovery", while the new grain itself undergoes accelerated work hardening as compared to the matrix. Numerical analysis using current simulation data reveals a macroscopic kinetic equation describing the average dislocation density evolution during DRX softening. The critical strain for the onset of DRX and the Zener–Hollomon parameter are found to obey a power law, with the model predicted exponent being consistent with that found in experiments. Temperature-dependence of the Avrami exponents have also been predicted using the simulation data, which agrees with the experimental finding. The population of grain boundaries and triple and quadruple junctions are shown to evolve with deformation and be temperature-dependent.

1. Introduction

The application of thermomechanical processing (TMP) for grain refinement and control of microstructure and texture in structural metals has continuously been advanced in industry and has been an active area of scientific research since the 1940's. In terms of both industrial application and scientific understanding, the combination of cold working followed by annealing at elevated temperatures, to induce nucleation and growth of new grains that replace the deformed materials via static recrystallization (SRX), is the most developed. In contrast, dynamic recrystallization (DRX) involves the nucleation and growth of new grains during deformation at elevated temperature ($>0.5T_m$), which plays critical roles in processing many engineering metals such as steels, Mg-alloys and Ni-base superalloys to name a few, but remains poorly understood, with the

* Corresponding author.
E-mail address: zhao.247@osu.edu (P. Zhao).

https://doi.org/10.1016/j.ijplas.2017.09.009
0749-6419/

lack of both fundamental knowledge and rigorous physics-based models in predicting the evolution of microstructure (e.g., dislocation density and grain structure) and the corresponding effects on the macroscopic stress-strain behavior (Sakai and Jonas, 1984; Rollett et al., 2004; Lin and Chen, 2011; Sakai et al., 2014). For instance, the determination of the critical strain for the onset of DRX would require successive interrupted tests and characterization, which makes systematic studies difficult for a given alloy. In addition, mean-field phenomenological rules/models (e.g., Ryan and McQueen (1990); Poliak and Jonas (1996); Mirzadeh and Najafizadeh (2010)) relying solely on analyzing the stress-strain behavior can only be valid to certain extent, as similar features may also be found in the stress-strain behavior during cold working (Zehetbauer and Seumer, 1993) where DRX is absent.

To fully utilize DRX in TMP for the optimization of properties closely related to the final grain structure, it is essential to establish better understanding and obtain more quantitative description of the underlying dynamic evolution of microstructural and micromechanical fields, which can be achieved using physics-based computational models. The key challenge for modeling DRX is the dynamic coupling between the internal micromechanical fields resulting from the applied mechanical load, which is highly non-uniform in polycrystals, and the dislocation field and grain structure, which keep evolving in response to the local stress field and in return influence the micromechanical fields. The overall stress-strain behavior is a result of the interplay between work hardening and softening due to dynamic recovery (DRV) and DRX. Note that DRX in this work refers to the *discontinuous* dynamic recrystallization where new grains evolve by nucleation and growth, as compared to the term *continuous* dynamic recrystallization that usually occurs during severe plastic deformation at relatively lower temperatures (Sakai et al., 2014). The development of previous models of DRX has shown a continued effort in incorporating more and more physical mechanisms involved in DRX (Ding and Guo, 2001; Takaki et al., 2008, 2014; Popova et al., 2015). Recently, we have developed an integrated model (Zhao et al., 2016) that fully couples a fast Fourier transform-based elasto-viscoplastic (FFT-EVP) model with a phase-field (PF) recrystallization model, with the incorporation of a dislocation-based description of work hardening and DRV and a stochastic model of DRX nucleation based on the grain boundary bulging mechanism (Beck and Sperry, 1950; Bailey and Hirsch, 1962).

In this study, we focus on the application of the model to investigating the evolution of both microstructural and micromechanical fields in polycrystal copper during uniaxial compression at various elevated temperatures. The current paper is organized as follows. In Section 2, the model framework is briefly reviewed. Section 3 presents the simulation results including hot compression tests at various temperatures, prediction on the critical strain of DRX, a DRX kinetic equation, and the evolution of microstructure and micromechanics during DRX. Further detailed analysis on the process and feature of DRX such as grain refinement, Avrami-type kinetics, necklace structure, and the concept of "DRX-enhanced recovery" are carried out in Section 4, which lead to better understanding of DRX mechanisms.

2. Method

2.1. Integrated modeling scheme

Our integrated model consists of three main parts: (1) deformation kinematics, which adopts the FFT-EVP model of Lebensohn et al. (2012), (2) a model-interface, which includes the dislocation-based constitutive theory of Ma et al. (2006) and our newly developed statistical model for DRX nucleation, and (3) a 3D PF recrystallization model extended from the model of Moelans et al. (2013). Since the construction and implementation of our DRX model has been fully described in Zhao et al. (2016), here we only present a diagram in Fig. 1 to illustrate the basic integration scheme and the readers interested in the details are referred to Zhao et al. (2016). It needs to be pointed out that the re-calculation of the stress field after PF simulation of the growth of new grains is critical as otherwise the stress field prior to DRX will not be concordant with the updated microstructure. The resulting stress redistribution will be shown to exhibit great influence on the neighboring grains and contribute significantly to the overall softening. In addition, the diffuse interfaces used in the PF model will be converted to sharp interfaces (via numerical binarization using an order parameter threshold of 0.5) before the microstructure is passed to the FFT-EVP model.

2.2. Temperature dependence of model parameters

The dislocation-based constitutive model employed here accounts for work hardening and DRV, and the temperature dependence is inherently built in via the use of thermally-activated deformation framework (Ma et al., 2006). The relevant parameters have been calibrated in Zhao et al. (2016), which exhibit the correct temperature dependence revealed by the experiments and will thus be directly used in the current work. Regarding the DRX nucleation model, the temperature dependence of parameters (e.g., the characteristic dislocation density for nucleation, exponent for Weibull distribution describing the critical nucleation strength, and grain boundary mobility) need to be taken into account, and their values used in the current work are listed in Table 1. In Zhao et al. (2016), it has been derived that the probability of nucleating a DRX grain at a FFT-CP gridpoint can be described using a two-parameter model

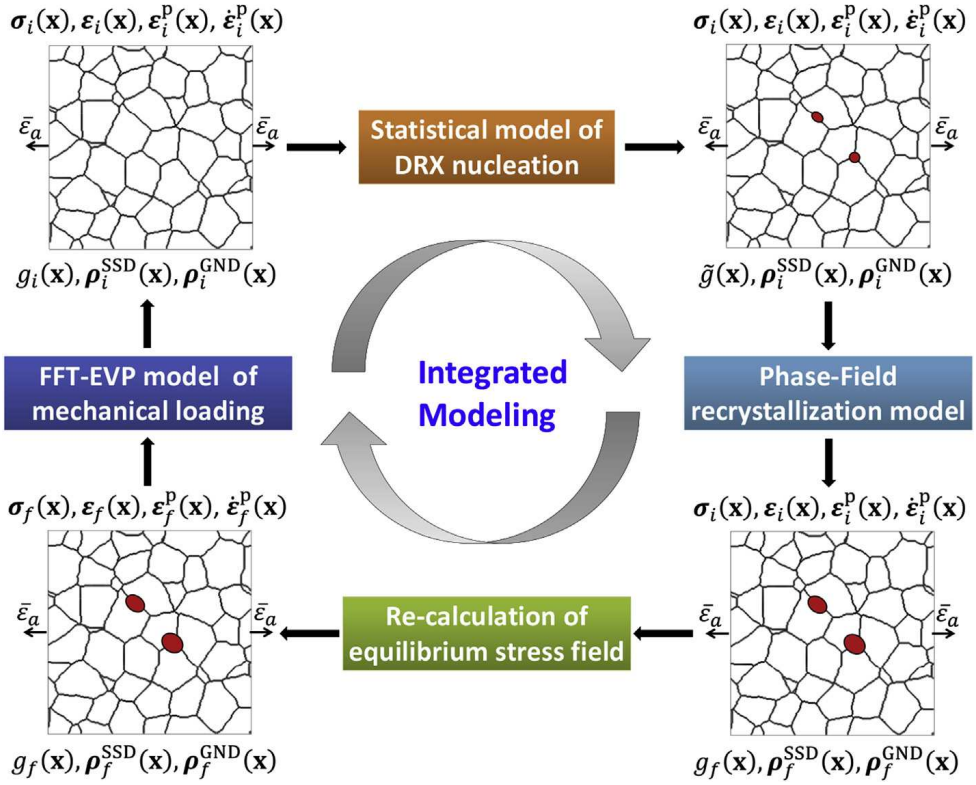

Fig. 1. Diagram illustrating the integrated modeling scheme to be used in the current work for simulating dynamic recrystallization. Within each simulation step, the model starts with an initial (the current) equilibrium micromechanical fields $(\boldsymbol{\sigma}_i(\mathbf{x}), \boldsymbol{\varepsilon}_i(\mathbf{x}), \boldsymbol{\varepsilon}_i^{\mathrm{p}}(\mathbf{x}), \dot{\boldsymbol{\varepsilon}}_i^{\mathrm{p}}(\mathbf{x}))$ and microstructural descriptors $(g_i(\mathbf{x}), \boldsymbol{\rho}_i^{\mathrm{SSD}}(\mathbf{x}), \boldsymbol{\rho}_i^{\mathrm{GND}}(\mathbf{x}))$, and ends up with the corresponding final (the updated) equilibrium fields (with a subscript f) that serve as the starting point for the next simulation step.

$$P = 1 - e^{-\left(\frac{k}{k_c}\right)^q}, \tag{1}$$

where k_c is the characteristic dislocation density for nucleation, q basically determines the shape of the distribution of DRX nucleation strength, and k is the local dislocation density predicted by the constitutive model and evolves with deformation. In Zhao et al. (2016), we have shown that

$$k_c = \left[C^{-1}\exp\left(\frac{Q_{\mathrm{DRX}}}{RT}\right)\right]^{1/q} \tag{2}$$

where C is a constant, Q_{DRX} is the apparent activation energy associated with DRX, R is the gas constant and T is temperature. The determination of k_c and q (especially its temperature dependence) relies on fitting the integrated model to existing DRX stress-strain curves. In the following simulation, we will use two sets of experimental data at two different temperatures (573K and 723K) to obtain the corresponding k_c and q, and then estimate the values at two intermediate temperatures (623K and 673K) to carry out simulations as complete predictions. According to Eq. (2), the constant C and Q_{DRX} are required for the estimation of k_c and q. While Q_{DRX} can be determined by experiments, C is related to the absolute value of nucleation rate (Zhao et al., 2016) and hence likely temperature-dependent. It is found further that the correlation between k_c and q and the temperature dependence of C are critical for the calibration of the model parameters. To account for the fact that the nucleation rate of DRX (and thus C) is larger at higher temperatures, we slightly increase q values at 623K and 673K while using a simple linear interpolation to estimate k_c at different temperatures. Another model parameter s_{nucl} accounts for the change of k_c (Zhao et al., 2016) and is here assumed to be linearly dependent on temperature as well. Currently parameters in the nucleation model at the prediction temperatures are essentially made by very crude estimation with only two experimentally calibrated data at the bounds. In future studies, we will further calibrate the model using experimental data at one or two additional temperatures where DRX is operating. In that case, more confidence will be gained for the parameters in Table 1 and the predictions will bear more quantitative significance. Nevertheless, the conclusion to be presented in the following sections should still be qualitatively correct.

Table 1
Material properties and parameters of nucleation and phase-field models for copper (†Murr (1975); ‡Vandermeer et al. (1997).).

Symbol [unit]	Value	Meaning
$\omega_{gb}^{\dagger}$ [J/m^2]	0.625	Grain boundary energy
$M_{gb}^{\ddagger}$ [m^4/(MJ·s)]	100 (573K)	Grain boundary mobility
	102 (623K)	
	130 (673K)	
	145 (723K)	
ζ	0.25	Constant for stored strain energy
k_c [10^{12}m^{-2}]	400 (573K)	Characteristic dislocation density for nucleation
	367 (623K)	
	333 (673K)	
	300 (723K)	
q	7.0 (573K)	Exponent for Weibull distribution of nucleation rate
	6.2 (623K)	
	5.8 (673K)	
	4.4 (723K)	
s_{nucl}	0.10 (573K)	Accounting for the change of k_c
	0.083 (623K)	
	0.067 (673K)	
	0.050 (723K)	
s_{soften}	0.9	Fraction of GND inherited in DRX grains

3. Results

The representative volume element (RVE) of the following simulations is constructed based on the texture information of the polycrystalline sample of 99.99% pure Cu (4N) used in the hot compression tests of Wusatowska-Sarnek et al. (2002), of which the experimental data will be directly compared with our simulation. The RVE has an average grain size of $\sim 230\mu$m and contains 191 grains initially. We use a 64^3 computational grid with a grid spacing of 21.4μm for the FFT-EVP modeling and refine the grid to 128^3 for the PF modeling. For more detailed information regarding the computational conditions, the readers are referred to Zhao et al. (2016).

3.1. Stress-strain curves

In our previous work (Zhao et al., 2016), the stress-strain curve at 473K without DRX and at 723K with DRX have been reproduced using the integrated model. Here we further apply the model to simulate hot compression at 573K, 623K, and 673K under the same test condition (with a constant strain rate of 1.6×10^{-3}/s). Fig. 2(a) shows the simulated stress-strain curves, together with some of the corresponding experimental data. For a systematic analysis, previous results of 473K and 723K have also been plotted in Fig. 2(a).

The experimental stress-strain curve at 573K exhibits a monotonic strain hardening without a peak stress, which is also true in the entire tested range (upto 120% compression) of the experiment (Wusatowska-Sarnek et al., 2002). Nevertheless, DRX occurs according to the experimental characterization, and as shown in Fig. 2(b), a standalone FFT-EVP simulation will

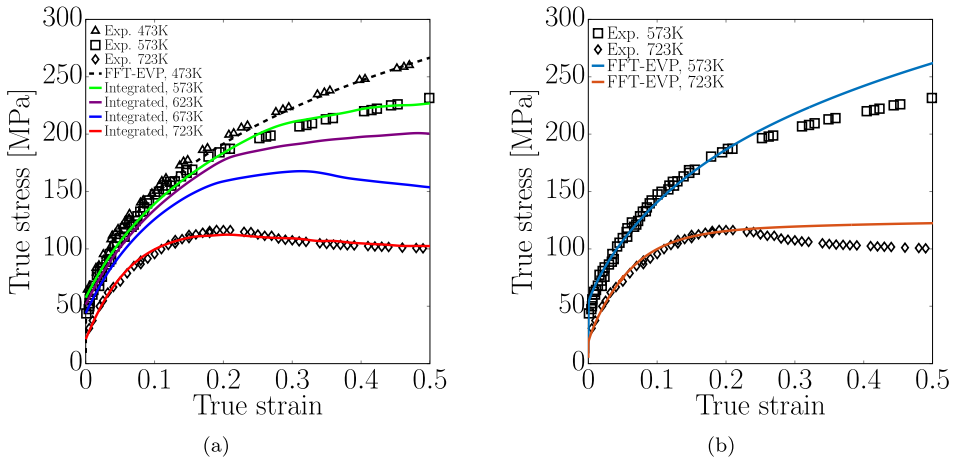

Fig. 2. Comparison between experimental (Wusatowska-Sarnek et al., 2002) and simulated stress-strain curves during uniaxial compression tests on polycrystalline copper. In (a) the integrated modeling is used to account for DRX, while in (b) standalone FFT-EVP simulation results are presented to show its incapacity in capturing DRX induced softening.

produce a stress-strain curve with higher flow stress than the experimental result. The integrated modeling, on the other hand, can reproduce the experimental stress-strain curve as shown in Fig. 2(a). The stress-strain curve at 623K appears to exhibit a nearly monotonic strain hardening as well in the simulated strain range, but actually has a peak stress at ~ 48% macroscopic strain. As the temperature increases to 673K, the simulated stress-strain curve shows clearly the presence of a peak stress, which is similar to the curve at 723K. Both results at 623K and 673K are complete predictions of the integrated model calibrated using the three sets of experimental data, and their validity and merit will be borne out in the following sections.

3.2. Onset of dynamic recrystallization

The critical strain ε_c corresponding to the onset of DRX has been shown to occur earlier than the peak strain ε_p (Luton and Sellars, 1969; Sakai and Jonas, 1984), which corresponds to the peak stress σ_p and is typically present in the DRX stress-strain curve. Since the stress-strain curve continues to show hardening after ε_c (especially in polycrystals), the presence of ε_p (σ_p) is often considered as the sole reliable indication of DRX initiation (Poliak and Jonas, 2003). Nevertheless, in many materials DRX occurs in the absence of peak stress in the stress-strain curves (e.g., the case of 573K shown in Fig. 2(a)). In such cases, the approach relying on a constant ratio between ε_c and ε_p (Manonukul and Dunne, 1999; Poliak and Jonas, 2003) to predict ε_c will fail. Our current model is calibrated solely using the experimental stress-strain curves at 473K and 723K, validated against the experimental stress-strain curve at 523K, and applied to the prediction of deformation at 623K and 673K. As a result, ε_c is considered as a direct prediction of the model. The value of ε_c for simulations in Fig. 2(a) are summarized in Table 2. According to Poliak and Jonas (2003), ε_c can be described as

$$\varepsilon_c = \xi B D_0^{n_d} Z^{n_c} \tag{3}$$

where ξ is a constant ratio (~ 0.5), D_0^p is the initial grain size, B, n_d, and n_c are material constants, and Z is the Zener–Hollomon parameter $Z \equiv \dot{\varepsilon}_{ap} \exp[Q/RT]$ with $\dot{\varepsilon}_{ap}$ being the applied strain rate and Q the apparent activation energy for the deformation. For our simulations with the same initial grain structure and applied strain rate, we would then expect

$$\ln\varepsilon_c = S + n_c \ln Z = S' + \frac{n_c Q}{R}\frac{1}{T} \tag{4}$$

where S and S' are constants. In Fig. 3, we apply Eq. (4) to fitting the predicted ε_c at four different temperatures. Using the experimentally measured apparent activation energy for dynamic recrystallization as 237 kJ/mol for polycrystal copper (Sample et al., 1987), it can be obtained from the fitting in Fig. 3 that $n_c = 0.130$, which is close to the value of 0.185 obtained by García (2004) based on experimental data of copper. The deviation in n_c is typical in analysis of other systems such as n_c =0.12–0.22 for Nb steels (Cho et al., 2001), which may be attributed to factors such as different test conditions, material compositions or purity. It also needs to be pointed out that as mentioned previously the material properties for simulations at 623K and 673K are obtained based on rough estimations, which may account for the deviation in n_c as well. Nevertheless, considering the fact that similar relationship as Eq. (3) and a value of n_c consistent with the experiment measurement have been obtained using the simulation data, the current model may indeed capture the underlying dynamics of DRX at mesoscale.

3.3. A macroscopic kinetic equation for DRX

It would be useful if we can establish a correlation between the observed macroscopic softening and microstructure, which is also of practical significance in terms of constitutive modeling of DRX at macroscopic level (similar to the usage of Kocks-Mecking model in many crystal plasticity simulations). We choose the average dislocation density as the key microstructure parameter to establish a kinetic equation accounting for softening of DRX. To this end, we first plot in Fig. 4 the average dislocation densities predicted by our model. It is seen that at 573K and 623K, while the statistically stored dislocation (SSD) and mobile dislocation densities are monotonically increasing, the geometrically necessary dislocations (GND) show a decrease in density after ~ 20% strain, which results from the softening due to DRX in our model. At 673K and 723K where DRX is more frequent due to larger thermal assistance, the SSD, GND, and mobile dislocations all decrease in density with increasing plastic deformation, as shown in Fig. 4. These results suggest that only when the deformation condition (e.g.,

Table 2
Simulated critical and peak stress/strain values, together with predictions (underlined numbers) on the missing values in the corresponding stress-strain curves.

Temperature [K]	ε_c	ε_p	$\varepsilon_c/\varepsilon_p$	σ_c [MPa]	σ_p [MPa]	σ_c/σ_p
723	0.06	0.22	0.27	81.5	112	0.73
673	0.098	0.32	0.30	125	167	0.75
623	0.13	0.48	0.27	150	201	0.75
573	0.24	<u>0.86</u>	<u>0.28</u>	197	<u>266</u>	<u>0.74</u>

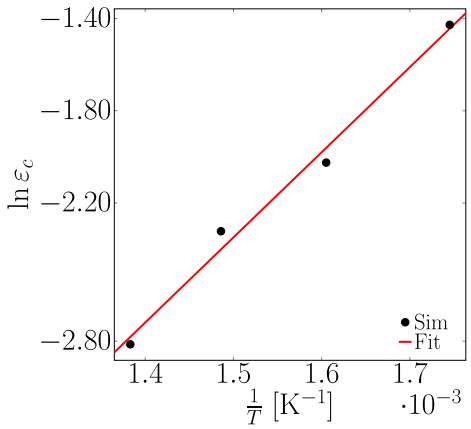

Fig. 3. Model prediction on the critical strain of DRX initiation at different temperatures. A linear fit is given to indicate the possible temperature dependence.

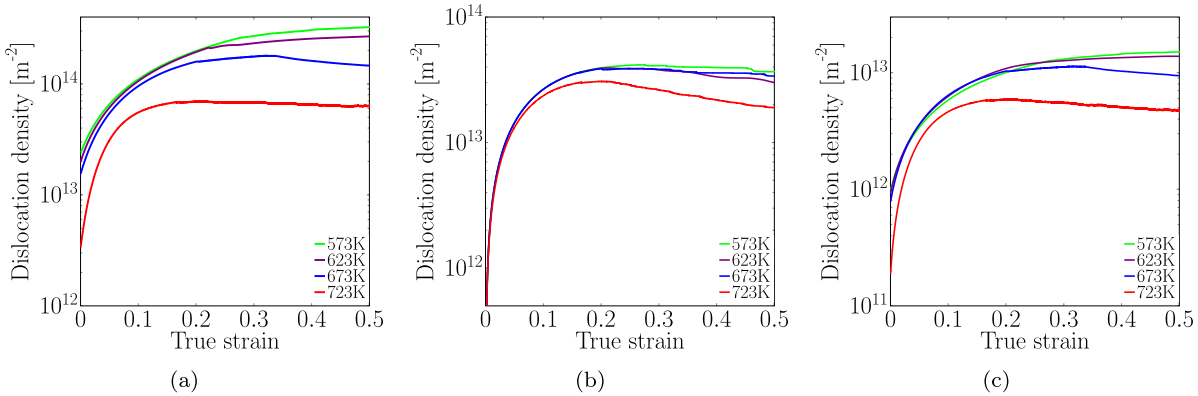

Fig. 4. Predicted density evolution of (a) SSD, (b) GND, and (c) mobile dislocations corresponding to the simulations in Fig. 2(a).

temperature) is such that DRX is promoted frequently enough can the softening outweigh the hardening to result in macroscopic softening. (In the next section, we will show the micro-mechanism of the correlation between the formation of DRX grains and the stress softening.)

At the macroscopic level, Sakai and Ohashi (1990) have proposed a scaling law between the peak stress σ_p and a mean-field critical dislocation density ρ_p for DRX nucleation, i.e., $\sigma_p \propto \sqrt{\rho_p}$. Then the stress decrement from σ_p to the steady-state flow stress σ_s, i.e., $\Delta\sigma$ is proposed to be

$$\frac{\Delta\sigma}{\sigma_p} = 1 - \sqrt{\frac{\rho}{\rho_p}}, \tag{5}$$

where ρ is the average dislocation density (including SSD, GND, and mobile dislocations) of a highly heterogeneously distributed dislocation substructures (Sakai and Ohashi, 1990; Sakai, 1995). It is obvious that according to Eq. (5), the critical dislocation density ρ_p for DRX nucleation in Sakai and Ohashi (1990) corresponds to the total dislocation density at the peak stress σ_p. This has not been confirmed in the original work of Sakai and Ohashi (1990) and Sakai (1995), for the evolution of dislocation density is difficult to obtain experimentally. In addition, the model (Eq. (5)) was only applied to the steady-state, virtually a single data point corresponding to the steady-state flow stress. Since after the peak stress the substructure will become significantly heterogeneous (Sakai and Ohashi, 1990; Sakai, 1995), it would be interesting to see if Eq. (5) can actually hold for the entire softening stage in the stress-strain curve.

Using the data predicted by our model, i.e., $\Delta\sigma$ (Fig. 2(a)) and ρ (Fig. 4(a) and (b), and 4(c)), we can actually apply Eq. (5) to the entire macroscopic softening regime and obtain ρ_p as the only fitting parameter in Eq. (5). Note that the peak stress appears at nearly the end of the simulation at 623K, and consequently no sufficient amount of data is available for $\Delta\sigma$ and ρ at 623K. As a result, the above analysis is only applied to the simulations at 673K and 723K. The fitting result shown in Fig. 5 exhibits a great consistency with the model of Sakai and Ohashi (1990), with the obtained ρ_p being 230.0 [10^{12} m^{-2}] for 673K and 105.9 [10^{12} m^{-2}] for 723K. By comparing with the dislocation density data in Fig. 4, it is further confirmed that the critical dislocation density ρ_p so obtained indeed corresponds to the total dislocation density at the peak stress σ_p. Our

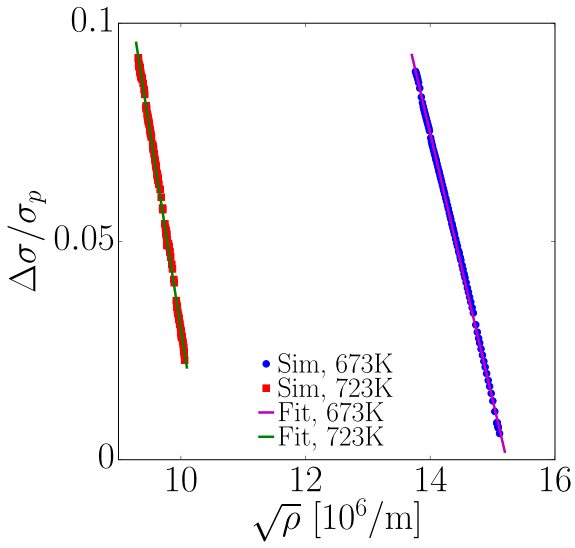

Fig. 5. Stress decrement as a function of dislocation density. The fitting parameter ρ_p according to the flow stress model in Eq. (5) is 230.0[10^{12} m^{-2}] for 673K and 105.9[10^{12} m^{-2}] for 723K.

analysis thus confirms that Eq. (5) can actually be applied to the entire softening regime of DRX to link the macroscopic stress behavior to the microscopic dislocation density evolution.

In addition, it was assumed in Sakai and Ohashi (1990) that the relationship $\sigma_p \propto \sqrt{\rho_p}$ holds approximately, even though the underlying dislocation structure is significantly heterogeneous. Following the Taylor hardening relation, we define a dimensionless constant

$$\alpha_p = \frac{\sigma_p}{\mu b \sqrt{\rho_p}} \tag{6}$$

where μ is the shear modulus and b is the magnitude of the Burgers vector. The value of α_p obtained from our current simulation are given in Table 3, indicating that α_p is indeed a material constant for the temperatures considered in the current work.

3.4. Stress redistribution around DRX grains

The predicted spatial distribution of stress components and plastic strain components by the full-field model are shown in Fig. 6, where only the diagonal components of the stress/strain tensor fields are shown for the current uniaxial compression simulation. For better visualization and analysis, only a 2D cross-section in the 3D computational cell is shown. It is obvious that the deformation is heterogeneous and localized considerably at GBs and grain junctions. Fig. 7 plots the corresponding dislocation density fields, which shows clearly localization at GBs and junctions, especially for GND and mobile dislocations shown in Fig. 7(b) and (c), respectively.

Since the dislocation density evolution is closely related to the softening, we show in Fig. 8 the change in the total dislocation density field from right before the nucleation of a DRX grain to after the new grain has grown (during concurrent deformation) to an equivalent radius of $\sim 85\mu$m. To isolate the effect of one individual DRX grain, the DRX event in Fig. 8 is chosen at the early stage (where nucleation is still a rare event) prior to the peak stress. Clearly there are mainly two local regions undergoing softening upon the DRX event, both of which are in the vicinity of the new grain rather than being located within it. This should be expected since the new grain has undergone much faster strain-hardening as it grows to the present size during deformation.

To better analyze the change in microstructural and micromechanical field, two 2D cross-sections as indicated in Fig. 8 are selected. In particular, the SSD density change distribution on the horizontal plane in Fig. 8 is shown in Fig. 9(a) and the GND density change distribution on the vertical plane in Fig. 8 is shown in Fig. 9(b). Grid points at which dislocation density decreases (i.e., local softening) are marked with dots in Fig. 9(a) and (b). It is seen that regions where SSD decreases actually coincide with those where the total dislocation density decreases as shown in Fig. 8, which is as expected since SSD constitutes the majority of the total dislocation density. Regions where GND decreases are more scattered in space with a trend of clustering more around the new grain. It has also been confirmed that after a few further loading increments those softening regions disappeared, for it is still prior to peak stress and strain hardening dominates the overall mechanical response before another DRX event occurs.

Table 3
Simulated data of σ_p and ρ_p in Eq. (5) together with the ratio $\alpha_p = \frac{\sigma_p}{\mu b\sqrt{\rho_s}}$.

Temperature [K]	ρ_p [10^{12}m^{-2}]	σ_p [MPa]	α_p
623	310.4	201.1	0.665
673	230.0	167.7	0.657
723	105.9	112.3	0.663

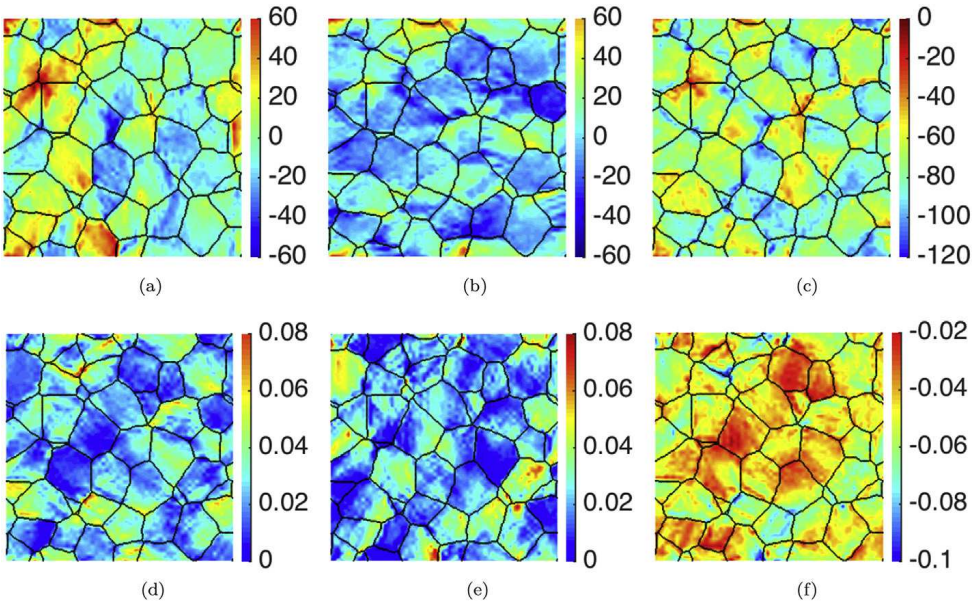

Fig. 6. Model prediction on stress component (a) σ_{xx}, (b) σ_{yy}, and (c) σ_{zz}, and accumulated plastic strain component (d) ε^p_{xx}, (e) ε^p_{yy}, and (f) ε^p_{zz} in a 2D cross-section plane perpendicular to the compression axis (z-axis). The plot corresponds to the simulation at 723K with a macroscopic strain of $\sim$ 5%. (The colorbar unit is MPa for the stress plot.) (For interpretation of the references to colour in this figure legend, the reader is referred to the web version of this article.)

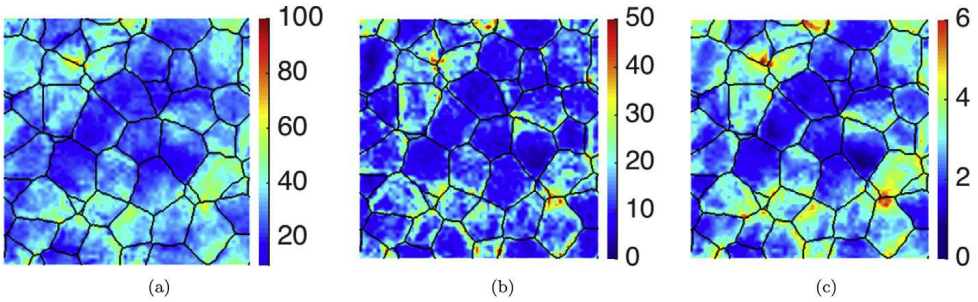

Fig. 7. Model prediction on the density of (a) SSD, (b) GND, and (c) mobile dislocation corresponding to the 2D cross-section plane in Fig. 6. (The colorbar unit is $10^{12}/\text{m}^2$.) (For interpretation of the references to colour in this figure legend, the reader is referred to the web version of this article.)

To reveal the correlation between the above softening and the stress redistribution, we plot in Fig. 9(c) and (d) the von Mises stress change (upon DRX event) corresponding to respectively Fig. 9(a) and (b). It is clearly shown in Fig. 9(c) that regions where SSD decreases (dots in Fig. 9(a)) actually experience the most significant stress decrease outside the new grain. On the other hand, the correlation between GND decrease and stress change is not apparent, which is reasonable because GND is more directly related to the strain gradient rather than to the stress.

3.5. Evolution of the population of grain boundaries and junctions

Another interesting quantitative prediction by the current simulations is the variation in the relative amount of grain boundaries and junctions (which largely determine the final mechanical properties). Since our FFT-based modeling relies on regular (simple) cubic grids, we categorize a gridpoint into the type of bulk, grain boundary, triple junction, or quadruple junction by comparing its grain ID with those of its nearest-neighbor gridpoints. Fig. 10(a) shows the evolution of the volume fraction of gridpoints belonging to those four types of microstructural features during DRX. As one would expect for grain

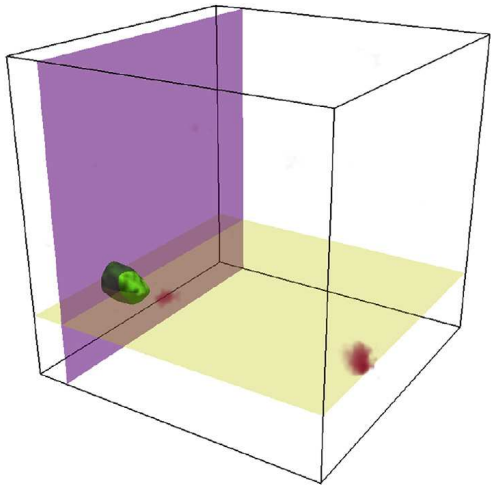

Fig. 8. Change in total dislocation density field upon the formation of a new DRX grain (green). Only sites with density decrease are colored in red. Two slice planes are used for 2D cross-section analysis in Fig. 9. (For interpretation of the references to colour in this figure legend, the reader is referred to the web version of this article.)

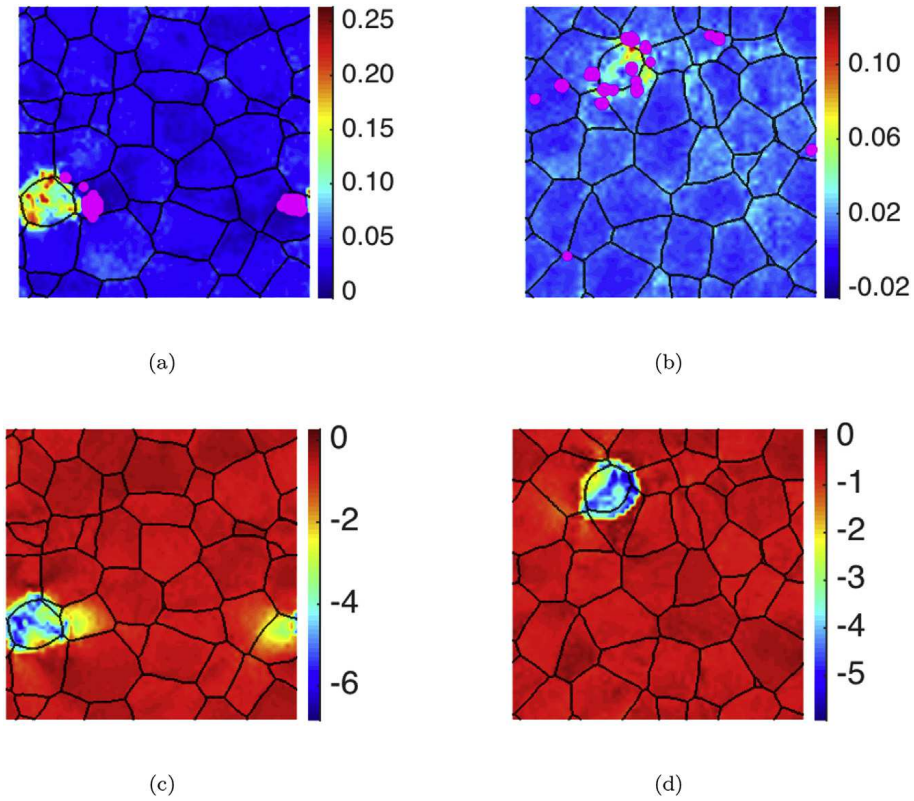

Fig. 9. 2D cross-section of (a) SSD and (b) GND density change in the horizontal and vertical planes respectively in Fig. 8, together with the corresponding change of von Mises stress shown respectively in (c) and (d). The colorbar unit is $10^{12}/m^2$ for (a) and (b) and MPa for (c) and (d). (For interpretation of the references to colour in this figure legend, the reader is referred to the web version of this article.)

refinement, the fraction of bulk gridpoints continues to decrease once DRX is initiated and that of grain boundaries and junctions keep increasing. To see the temperature effect on the population of those defects introduced by DRX, we consider the relative volume fractions of GB, triple junction, and quadruple junction in the material undergoing the same macroscopic deformation (5%) at different temperatures, and the results are shown in Fig. 10(b). In general, the total amount of new grain boundaries and junctions introduced by DRX increase as the deformation temperature increases. In addition, this temperature dependence is obviously nonlinear in nature according to Fig. 10(b), as when temperature is above 673K, the relative portion of grain junctions increases much faster than the case when the temperature is below 673K. Such nonlinearity is

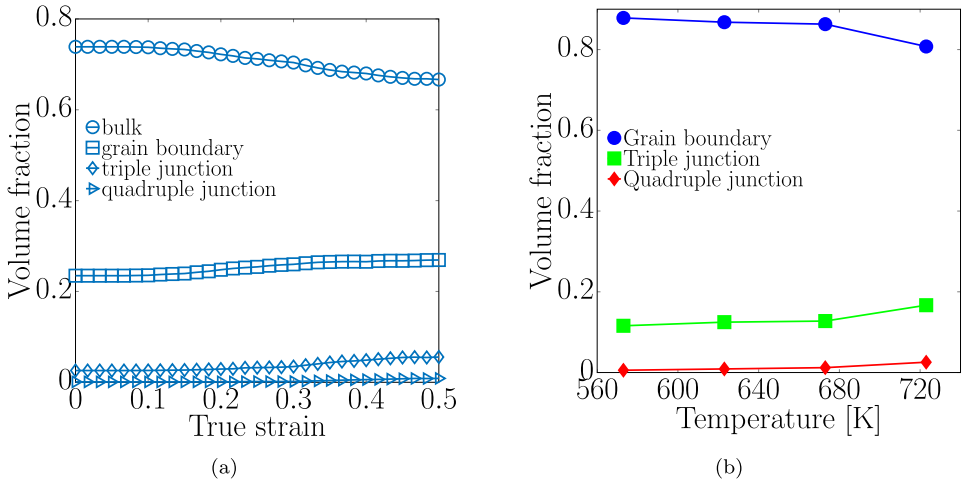

Fig. 10. Evolution of (a) volume fraction of gridpoints belonging to bulk, grain boundary, triple junction, or quadruple junction during hot deformation at 723 K, with the relative volume fractions of the latter three types shown in (b) for different temperatures at the same macroscopic compression (5%).

expected to result from the Arrhenius-type thermally activated process (e.g., grain boundary bulging mechanism) during the formation of DRX grains.

4. Discussion

4.1. Grain size evolution and transformation kinetics

Microstructural evolution is a direct prediction of the current integrated modeling. Fig. 11 presents some quantitative information related to the microstrucrual evolution, i.e., the mean grain size of the RVE and volume fraction of the recrystallized grains during the simulations. The overall grain refinement occurs at all three temperatures, which is also revealed by the experiments (Wusatowska-Sarnek et al., 2002). At 573K, 623K, and 673K, there appears to be some increase of the mean grain size at certain true strain levels when the true strain increases, which is due to the fact that the mean grain size shown here is simply determined by the total number of grains and there are instances where a new grain can grow quickly and consume completely some small old grains in its neighborhood. This situation is more likely to happen at lower temperatures and earlier stages when large stored energy is accumulated at certain local regions due to heterogeneous deformation, which provides a relatively large driving force to grow the new grains that happen to nucleate at these sites. It is also interesting to note that the simulated grain refinement process exhibits some "pop in" events where the mean grain size shows a sudden considerable decrease in all four cases shown in Fig. 11(a). Since as mentioned above the mean grain size is calculated based on the total number of grains, those "pop in" events implies a sudden formation of large amount of new grains, which results from the complicated coupling between grain structure evolution, dislocation density evolution, and new grain nucleation. It is also noted that these "pop in" events occur at certain time intervals as shown in Fig. 11(a), which leads to oscillations in the

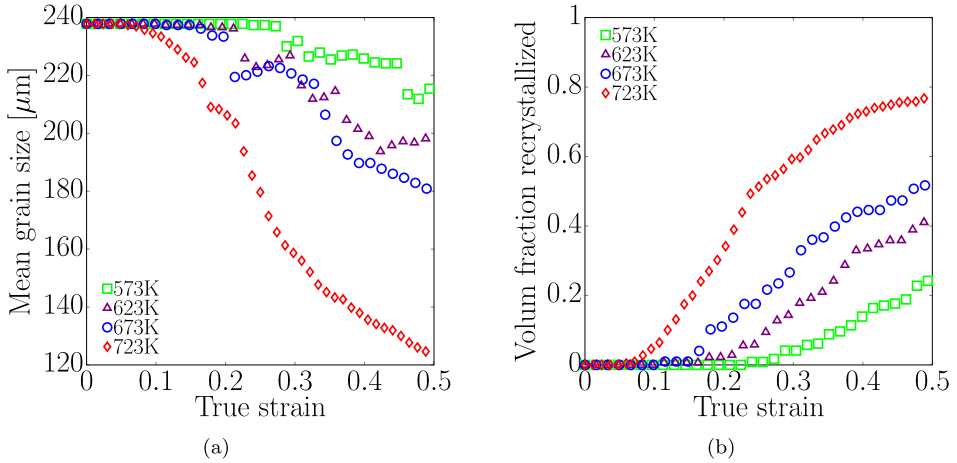

Fig. 11. Evolution of (a) mean grain size and (b) volume fraction of recrystallized grains during the integrated modeling at 573K, 673K, and 723K.

plots of volume fraction of the recrystallized grains against the true strain as shown in Fig. 11(b). Because of these oscillations, the volume fraction may not saturate at what it seems to be now in Fig. 11(b).

The temperature dependence of recrystallization kinetics shown in Fig. 11(b) agrees qualitatively with the expectation that DRX takes place more rapidly at higher temperatures. More quantitative analysis can be obtained by using the Avrami equation

$$X = 1 - \exp[-Bt^m], \tag{7}$$

where X is the volume fraction recrystallized, t is time, m is a constant called Avrami exponent, and B is a temperature-dependent constant. For DRX tests with a constant strain rate $\dot{\varepsilon}$, t in Eq. (7) is usually replaced by $t = (\varepsilon - \varepsilon_c)/\dot{\varepsilon}$ (Roberts et al., 1979), and the Avrami exponent is given by $m = \frac{\partial \ln[-\ln(1-X)]}{\partial \ln t}$. Fig. 12 shows the fitting results using Eq. (7) and the corresponding Avrami exponent for different temperatures. It is seen that the fitting value of m is in the range of $1.2 \sim 1.4$, which is consistent with some experimental measurement on commercial purity copper as shown in Table 4. While m at 673K is slightly smaller than that at 623K in our current work, overall we see that m increases with increasing temperature. The same temperature-dependence of m has also been seen in an experimental work on commercial purity copper (García et al., 2000). As a comparison, experimentally measured Avrami exponents for other metallic systems are also collected and listed in Table 4. The fact that most of the experimentally measured m for diverse systems fall into $(1, 2)$ suggests that the prediction of DRX kinetics may essentially rely on faithfully capturing the concurrent nucleation and growth (encoded in the stress-strain curves) without involving the detailed alloy chemistry. As a result, our current model may be applied to the study of DRX with a broader scope.

4.2. Microstructural features of DRX

For better visualization of the grain structure during DRX, Fig. 13 plots the {1 1 1} cross-sections (in the sample reference frame) during the simulated DRX process at 723K. It is seen that new grains continue to bulge out from grain boundaries and junctions and grow to replace old grains. Some of these boundaries and junctions due to the formation of new grains have been indicated by the white dotted lines in Fig. 13. The formation of new grains occurs heterogeneously and repeats itself over the deformation, as fresh DRX nuclei (small new grains) distributed along GBs can be identified at the later stages as indicated by the yellow dotted lines in Fig. 13. Such "necklace" structure has been proposed by theory and observed by experiments (Rollett et al., 2004). It needs to be pointed out that according to our simulation, the necklace structure becomes more frequently observed only after certain deformation post ε_c (which can be much smaller than the experimentally determined value as discussed in Section 3.2). From a statistical point of view, it is difficult to find a necklace structure when DRX is still a rare event, and the necklace shape may be highly non-uniform as shown Fig. 13. In addition, our simulation suggests that the DRX volume does not proceed via continuous and consecutive formation of the necklace structures as proposed by some theory (Rollett et al., 2004), but exhibits a strong stochastic nature as shown in Fig. 13, which is also supported by some experiment (Ponge and Gottstein, 1998). This may be related to the fact that the boundaries between the initial parent grains and between the parent and DRX grains are different in terms of features such as the local plastic strain and dislocation density. Finally, experimental analysis suggests that the microtexture of these necklace grains, especially at the early stage of the deformation, have orientations akin to those of the parent grains (Ponge and Gottstein, 1998), which supports our current model assumption that DRX grains will inherit the textures of the parent grains.

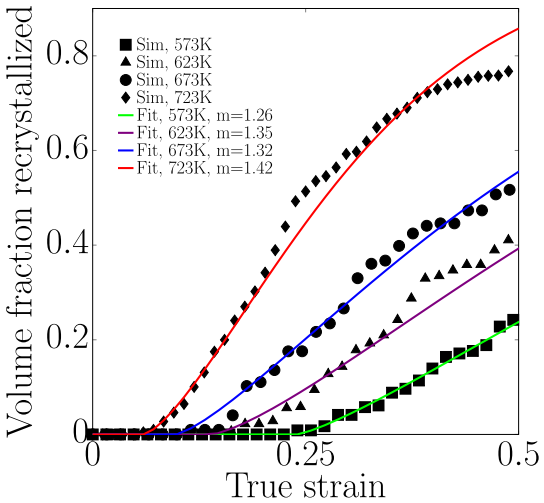

Fig. 12. Analysis of DRX transformation kinetics data from simulation using Avrami equation (Eq. (7)).

Table 4
Avrami exponent for DRX in various alloys.

Alloy	Avrami exponent m
Commercial purity copper	1.0–2.4 (García et al., 2000)
4N copper	1.2–1.4 (current simulation)
AISI 304, 4439	1.2–1.3 (Roberts et al., 1979)
Nickle	0.9 (Sah et al., 1974)
α iron	1-2 (Glover and Sellars, 1972)
IN718	1.68–1.9 (Na et al., 2003)
High Nb containing TiAl	0.9–1.1 (Cheng et al., 2013)
Waspaloy (as cast)	1.65–3.49 (Semiatin et al., 2004)

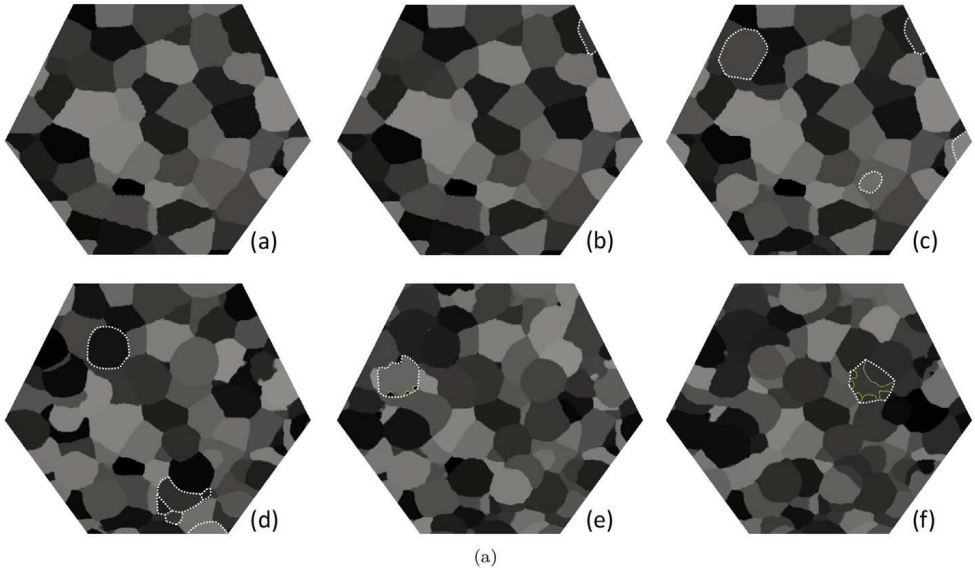

Fig. 13. Grain map (colored by the grain ID) on a {111} cross-section at the strain of (a) 0%, (b) 9.6% (c) 14.4%, (d) 26.3%, (e) 38.2%, and (f) 50.0% during the integrated modeling at 723 K. (For interpretation of the references to colour in this figure legend, the reader is referred to the web version of this article.)

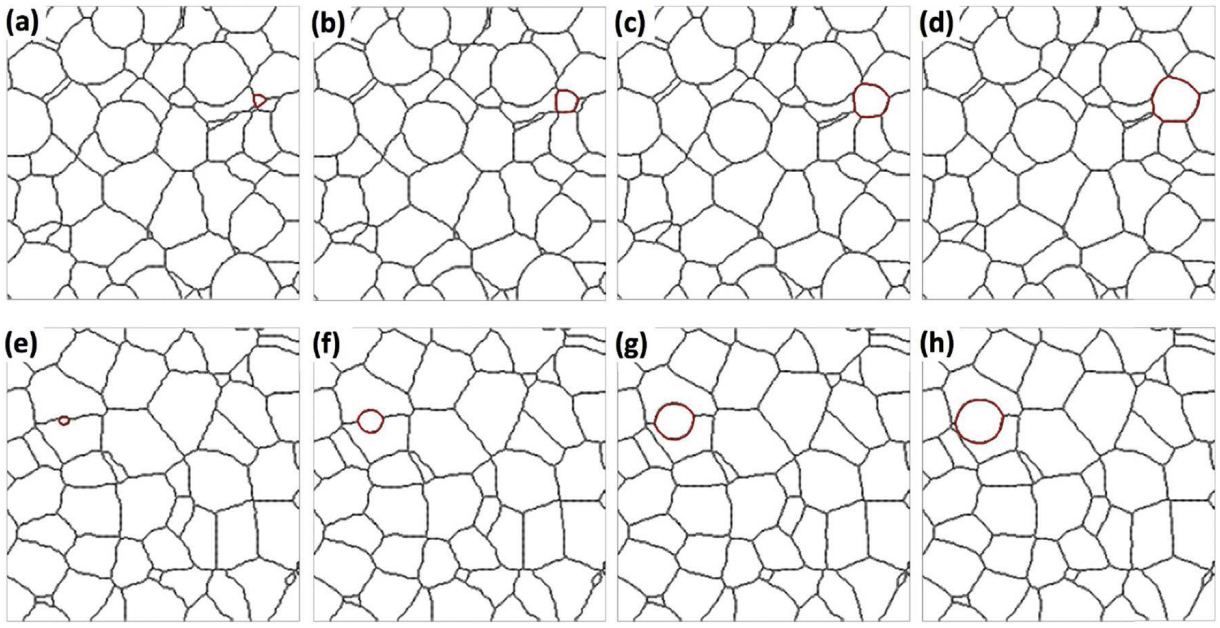

Fig. 14. 2D cross-section of grain structures showing the formation of new grains at (a–d) a triple junction and (e–h) a normal boundary, obtained, respectively, from integrated simulation at 723K and 573K. The duration of the exhibited dynamics (from left to right column) corresponds to a physical time of 0.02s (top row) and 0.027s.

In order to obtain more detailed microstructural features during DRX nucleation and growth, we plot in Fig. 14 the successive steps of two new grains formed at respectively a grain boundary and a triple junction. At the triple junction, the DRX grain initially exhibits a triangular shape (in 2D cross-section) as shown in Fig. 14 (a), and later on grows into an irregular sphere by consuming the neighboring grains, which is due to the different deformation energy stored in each grain as indicated by the heterogeneously distributed dislocation density shown in Fig. 7. Note that this new grain is formed in the early stage of DRX and there is no impingement effect from other DRX grains. For the DRX grain formed at the grain boundary, the new grain is initially bulged out mainly within one grain (Fig. 14(e)), which is consistent with many experiments (Ponge and Gottstein, 1998; Wusatowska-Sarnek et al., 2002; Miura et al., 2007). Nevertheless, the new grain quickly grows into grains on both sides of the boundary and exhibits a smooth spherical shape as shown in Fig. 14(f)-(h), which is different from the case at the triple junction. It also needs to be pointed out that the grain boundary properties are assumed isotropic in the current model; if boundary anisotropy (depending on the crystallographic orientations) is further introduced, the simulated DRX grains at grain boundaries may also exhibit irregular shapes as shown in experiments.

Finally, a GB velocity of $\sim 1 \times 10^3 \mu$m/s at 723 K is also estimated from Fig. 14. Theoretically, the GB velocity is given as (Vandermeer et al., 1997)

$$v_{\mathrm{GB}} = \frac{\Delta f}{d_a} \cdot V_a \cdot \frac{D_b}{RT} \tag{8}$$

where Δf is the instantaneous driving force for GB migration, d_a is the inter-atomic jump distance, V_a is the atomic volume, and D_b has an Arrhenius temperature-dependence with the same activation energy as that of the GB diffusivity. Experimental measurement of GB velocity shows a strong dependence on the purity as well as the boundary type, and consequently the pre-factor of the Arrhenius expression of D_b can vary by two orders of magnitude. Using a typical driving force $\Delta f \sim 1$ MPa (Vandermeer et al., 1997) and an activation energy (for GB diffusion) of 104 kJ/mol (Buehler et al., 2004), it is estimated that the v_{GB} at 723K is $[10, 1000]\mu$m/s (depending on the value of the pre-factor). Our estimation from Fig. 14 meets the upper bound of this range. The lower boundary value is supported by experimental values of a 18° tilt boundary (Viswanathan and Bauer, 1973). Note that the GB energy and mobility in our model are assumed constant and independent of misorientation. With more realistic consideration of GB structure-property relationship and the corresponding database, our model should be able to predict more reasonable and accurate GB migration.

4.3. DRX-enhanced recovery

The results in Figs. 8 and 9 and the analysis confirm quantitatively that stress redistribution due to strain compatibility upon the formation of DRX grains can have a profound influence on the subsequent dislocation evolution and softening, as has been suggested in our previous work (Zhao et al., 2016). Since our model resides in time and length scales that are much larger than those associated with a critical nucleus of DRX grains (Sakai and Ohashi, 1990; Sakai, 1995), only the GND content is lowered but the SSD content remains unchanged during the microstructural update upon DRX events (see Zhao et al. (2016) for the underlying physical consideration). As a result, the predicted correlation between stress redistribution and SSD content evolution as shown in Fig. 9 must confirm that stress redistribution upon local DRX events can indeed result in the overall softening behavior. In other words, in addition to the dynamic recovery that operates at the length scale of mean-free path of dislocations, there is another recovery process induced by DRX, i.e., “DRX-enhanced recovery”, which operates at the grain scale via the redistributed long-range internal stress field. Recently, Chauve et al. (2015) has analyzed the redistribution of strain and stress field during DRX nucleation in ice using Digital Image Correlation technique, which has become an advanced characterization tool for quantifying deformation, and could be used in future to make a quantitative comparison with the current results.

The DRX-enhanced recovery can be seen more clearly in Fig. 15 where the stress component change along a probe line across the new grain is plotted according to the simulation results in Section 3.4. The long-range elastic interaction can result in a change of $\sim$ 1MPa in grains (and near boundaries) that are a few grains away from the location of the newly formed grain. Note that the overall stress drop from the peak stress to steady-state flow stress is only $\sim 1 - 10$ MPa as shown in Fig. 2(a).

The concept of DRX-enhanced recovery can be further verified by analyzing the subsequent dynamics of dislocation evolution that controls the hardening and DRV. In Fig. 16 we plot the density evolution rate of SSD and two types of GND (i.e., screw-type and edge-type, see Zhao et al. (2016) for more details of the definition) before and after the formation of a new grain corresponding to Fig. 8. (Note that only one out of the twelve slip systems is shown in Fig. 16 and it is confirmed that the other slip systems exhibit similar features to be discussed below.) Since the plastic shear rate on each slip system has an exponential dependence on the resolved shear stress, and since the dislocation density evolution rates depend on the plastic shear rate and stress based on the dislocation multiplication and annihilation mechanisms (Ma et al., 2006), it is expected that the stress redistribution may significantly change the dislocation dynamics as now shown in Fig. 16. Before the formation of the DRX grain, the distribution of SSD (Fig. 16(a)) suggests an overall hardening behavior, of which the rate differs significantly from one grain to another due to different orientations. After the DRX grain is formed, the redistributed stress field changes the hardening rate drastically. In particular, grains that initially experience dislocation accumulation now start to have a net dislocation annihilation rate, i.e., the phenomenon of DRX-enhanced recovery, which is in particular the case in the neighboring grains of the DRX grain. In addition, the maximum rate of dislocation accumulation is also present mainly in the DRX

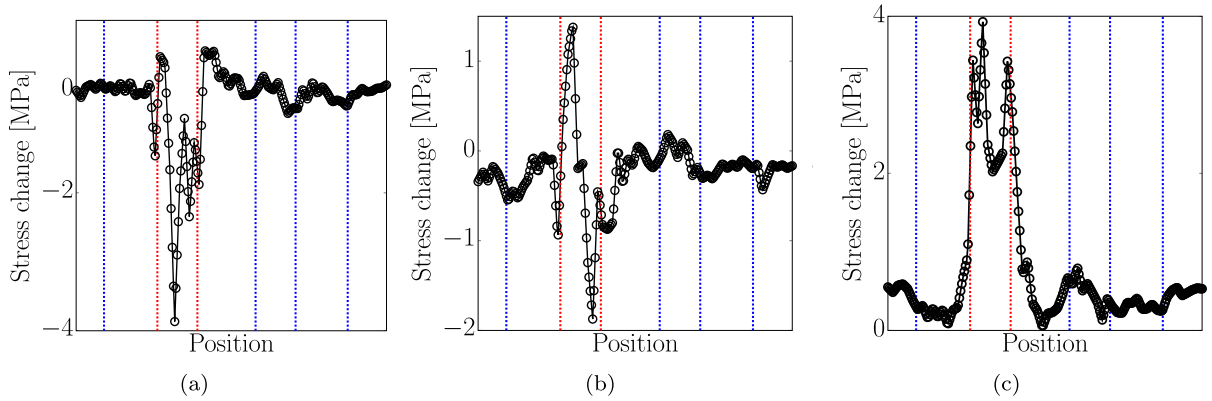

Fig. 15. Variation of stress change for (a)σ_{xx}, (b)σ_{yy}, and σ_{zz} along a probe line across the new grain in Fig. 8. The position of grain boundaries are indicated by the dashed lines: blue for boundaries of old grains and red for boundaries of the DRX grain. (For interpretation of the references to colour in this figure legend, the reader is referred to the web version of this article.)

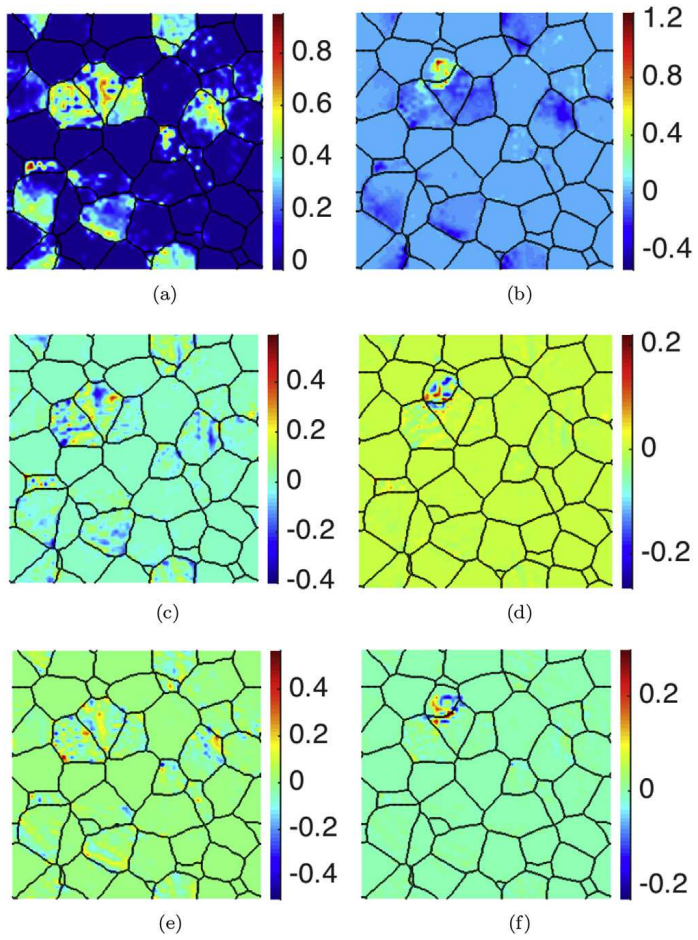

Fig. 16. Distribution of dislocation density evolution rate before (left column) and after (right column) the formation of a new grain corresponding to Fig. 8. One out of twelve slip systems is shown, including the rate of SSDs (top row), screw-type GNDs (middle row), and edge-type GNDs (bottom row) (Zhao et al., 2016). (The colorbar unit is $10^{12}/(m^2 \cdot s)$.) (For interpretation of the references to colour in this figure legend, the reader is referred to the web version of this article.)

grain, suggesting that new grains will harden much faster than the matrix in the subsequent deformation, as suggested by experiments (Sakai and Ohashi, 1990). Similar features can be found in the density evolution rate changes of GNDs in Fig. 16, which is determined by the gradient of plastic shear rates (Zhao et al., 2016). The corresponding maximum rate of GND annihilation/accumulation is again found within or near the new grain; some grains that are a few grains away from the DRX grain experience a drastic change in the GND density evolution rate as well. It can thus be concluded that DRX (occurring at

the grain scale) can influence dislocation density evolution (occurring at the subgrain scale) in the neighboring grains through stress redistribution and thus lead to DRX-enhanced recovery.

4.4. Scaling relationships of DRX

The scaling relationships among the characteristic features of the DRX stress-strain curves, i.e., ε_c, ε_p, σ_c (stress corresponding to ε_c), and σ_p are always of great practical importance. For example, as mentioned earlier, a constant ratio of $\varepsilon_c/\varepsilon_p$ and σ_c/σ_p have been indicated as a convenient way of determining the onset of DRX (Manonukul and Dunne, 1999; Poliak and Jonas, 2003; Najafizadeh and Jonas, 2006).

In Table 5 we summarize some experimental values of $\varepsilon_c/\varepsilon_p$ and σ_c/σ_p during DRX of several alloy systems, together with our current simulation results at 623K, 673K and 723K (where a peak stress is present) from Table 2. Note that while a constant ratio of $\varepsilon_c/\varepsilon_p$ and σ_c/σ_p has been seen in both experiments and simulations, their values are generally system-dependent, indicating that $\varepsilon_c/\varepsilon_p$ and σ_c/σ_p contain some material properties. In addition, since the detection of ε_c in our simulations should always be much earlier than the interrupted characterization used in experiments, our predicted ratios should always be smaller than that obtained from experiments, as shown in Table 5.

For the simulation result obtained at 573K, there is no peak stress present, and consequently $\varepsilon_c/\varepsilon_p$ and σ_c/σ_p cannot be defined. This has also been noted during the analysis of experimental DRX curves (Poliak and Jonas, 2003). Nevertheless, we may use the constant ratio in Table 5 to predict the peak stress and peak strain at 573K. These predictions are shown as underlined numbers in Table 2, which shows $\varepsilon_p = 0.86$ and $\sigma_p = 266$MPa at 573K. In the original experiment (Wusatowska-Sarnek et al., 2002), while there was no peak strain present up to a 120% compression, the stress started to saturate after a strain value of 0.86, and the saturated stress is ~ 250 MPa, slightly smaller than the predicted σ_p above using the constant ratio in Table 5. This discrepancy has also been found in the analysis of experimental DRX data by Poliak and Jonas (2003), where a larger ratio of σ_c/σ_p is obtained when σ_p is taken as the saturated stress when the peak is absent. The above analysis indicates that the missing peak in the stress-strain curves may be related to the breakdown of the previously established scaling laws in DRX.

4.5. Outlook

The current simulations have a few limitations that should be addressed in our future work. First, the scaling procedure used in dealing with the scale separation issue of DRX nucleation may be avoided by carrying out special simulations at a much finer scale to obtain directly the dislocation density in the new grain as function of its size. In addition, the temperature dependent nucleation model parameters can be further calibrated using more experimental stress-strain curves. Moreover, anisotropic grain boundary properties such as grain boundary mobility and energy can be introduced to account for more realistic DRX grain shapes and kinetics during growth. Finally, the orientation of new grains is assumed to adopt that of the old grains according to the conventional bulging mechanism but may actually be correlated with the local elastic or plastic state at the nucleation stage, as proposed previously by some simulations (Tóth and Jonas, 1992; Hildenbrand et al., 1999) and indicated recently by some experiments (Schulson et al., 2009; Duval et al., 2012). This is critical to understanding the texture evolution (especially the texture randomization) during DRX and can also be studied using the current integrated model.

5. Conclusions

In this paper, the microstructural and micromechanical field evolution during dynamic recrystallization (DRX) in polycrystal copper is investigated using our recently developed model that integrates a fast Fourier transform-based elasto-viscoplastic (FFT-EVP) model and a phase-field (PF) recrystallization model. Based on the predicted stress-strain behaviors of DRX at different temperatures together with the corresponding full-field microstructural and micromechanical data, the following major findings have been obtained through detailed quantitative analysis.

1. The correlation between stress redistribution upon the formation of new grains and the local dislocation density decrease in neighboring grains has been confirmed quantitatively for the first time. This dynamic picture offers a new (more physical) way of understanding the origin of softening due to DRX. In particular, a DRX-enhanced recovery process revealed by the current simulations is believed to be responsible for the micro-mechanism of DRX softening.

Table 5
The ratio of $\varepsilon_c/\varepsilon_p$ and σ_c/σ_p for DRX in various alloys.

Alloy	$\varepsilon_c/\varepsilon_p$	σ_c/σ_p
Commercial purity copper	0.63–0.68	0.91–0.94 (Manonukul and Dunne, 1999)
Commercial purity copper	0.28[a]	0.74[a] (current simulation)
Steels	0.3–0.8	$\sim$ 0.8(Poliak and Jonas, 2003)

[a] The simulation prediction should always be smaller than the experimental measurement.

2. A macroscopic kinetic equation for DRX softening has been revealed, which cannot be described by the Kocks-Mecking model. It is suggested that an additional DRX-enhanced recovery term has to be introduced into the conventional Kocks-Mecking model to consider simultaneous work hardening, dynamic recovery, and DRX, allowing DRX to be modeled at a macroscopic level in a physics-based manner.
3. The simulated critical strain for DRX initiation and the corresponding Zener–Hollomon parameter are found to obey a power law, with the predicted exponent consistent with that obtained from experiments.
4. The microstructural features during nucleation and growth of new grains are analyzed in details; the transformation kinetics and temperature-dependent Avrami exponents are obtained; the evolution of the population of grain boundary and junctions during DRX, together with their temperature dependence are predicted, which could be of great importance for assessing the correlation between DRX and properties.

Acknowledgments

This work is supported by the National Energy Technology Laboratory under Grant No. DE-FE0027776 (P.Z., Y.W. and S.R.N.), the National Science Foundation DMREF program under Grant No. DMR-1534826 (Y.W. and S.R.N.), and the National Science Foundation CMMI program under Grant No. CMMI-1662646 (S.R.N. and Y.W.).

References

Bailey, J., Hirsch, P., 1962. The recrystallization process in some polycrystalline metals. In: Proceedings of the Royal Society of London A: Mathematical, Physical and Engineering Sciences. The Royal Society, pp. 11–30.
Beck, P.A., Sperry, P.R., 1950. Strain induced grain boundary migration in high purity aluminum. J. Appl. Phys. 21, 150–152.
Buehler, M.J., Hartmaier, A., Gao, H., 2004. Constrained grain boundary diffusion in thin copper films. In: MRS Proceedings. Cambridge Univ Press, pp. P1–P2.
Chauve, T., Montagnat, M., Vacher, P., 2015. Strain field evolution during dynamic recrystallization nucleation; a case study on ice. Acta Mater. 101, 116–124.
Cheng, L., Chang, H., Tang, B., Kou, H., Li, J., 2013. Deformation and dynamic recrystallization behavior of a high nb containing tial alloy. J. Alloys Compd. 552, 363–369.
Cho, S.H., Kang, K.B., Jonas, J.J., 2001. The dynamic, static and metadynamic recrystallization of a nb-microalloyed steel. ISIJ Int. 41, 63–69.
Ding, R., Guo, Z., 2001. Coupled quantitative simulation of microstructural evolution and plastic flow during dynamic recrystallization. Acta Mater. 49, 3163–3175.
Duval, P., Louchet, F., Weiss, J., Montagnat, M., 2012. On the role of long-range internal stresses on grain nucleation during dynamic discontinuous recrystallization. Mater. Sci. Eng. A 546, 207–211.
García, V., 2004. Constitutive Relations to Model the Hot Flow of Commercial Purity Copper. Ph.D. thesis. Tesis de doctorado, Universidad Politécnica de Cataluña.
García, V., Cabrera, J., Riera, L., Prado, J., 2000. Hot deformation of a commercial purity copper. In: Proceedings of Euromat 2000: Advances in Mechanical Behaviour, Plasticity and Damage. Elsevier Science, Oxford, pp. 1357–1362.
Glover, G., Sellars, C., 1972. Static recrystallization after hot deformation of α iron. Metall. Trans. 3, 2271–2280.
Hildenbrand, A., Tóth, L., Molinari, A., Baczynski, J., Jonas, J., 1999. Self-consistent polycrystal modelling of dynamic recrystallization during the shear deformation of a ti if steel. Acta Mater. 47, 447–460.
Lebensohn, R.A., Kanjarla, A.K., Eisenlohr, P., 2012. An elasto-viscoplastic formulation based on fast Fourier transforms for the prediction of micromechanical fields in polycrystalline materials. Int. J. Plasticity 32, 59–69.
Lin, Y., Chen, X.M., 2011. A critical review of experimental results and constitutive descriptions for metals and alloys in hot working. Mater. Des. 32, 1733–1759.
Luton, M., Sellars, C., 1969. Dynamic recrystallization in nickel and nickel-iron alloys during high temperature deformation. Acta Metall. 17, 1033–1043.
Ma, A., Roters, F., Raabe, D., 2006. A dislocation density based constitutive model for crystal plasticity fem including geometrically necessary dislocations. Acta Mater. 54, 2169–2179.
Manonukul, A., Dunne, F., 1999. Initiation of dynamic recrystallization under inhomogeneous stress states in pure copper. Acta Mater. 47, 4339–4354.
Mirzadeh, H., Najafizadeh, A., 2010. Prediction of the critical conditions for initiation of dynamic recrystallization. Mater. Des. 31, 1174–1179.
Miura, H., Sakai, T., Mogawa, R., Jonas, J., 2007. Nucleation of dynamic recrystallization and variant selection in copper bicrystals. Philos. Mag. 87, 4197–4209.
Moelans, N., Godfrey, A., Zhang, Y., Jensen, D.J., 2013. Phase-field simulation study of the migration of recrystallization boundaries. Phys. Rev. B 88, 054103.
Murr, L.E., 1975. Interfacial Phenomena in Metals and Alloys. Addison-Wesley.
Na, Y.S., Yeom, J.T., Park, N.K., Lee, J.Y., 2003. Simulation of microstructures for alloy 718 blade forging using 3d fem simulator. J. Mater. Process. Technol. 141, 337–342.
Najafizadeh, A., Jonas, J.J., 2006. Predicting the critical stress for initiation of dynamic recrystallization. ISIJ Int. 46, 1679–1684.
Poliak, E., Jonas, J., 1996. A one-parameter approach to determining the critical conditions for the initiation of dynamic recrystallization. Acta Mater. 44, 127–136.
Poliak, E., Jonas, J., 2003. Initiation of dynamic recrystallization in constant strain rate hot deformation. ISIJ Int. 43, 684–691.
Ponge, D., Gottstein, G., 1998. Necklace formation during dynamic recrystallization: mechanisms and impact on flow behavior. Acta Mater. 46, 69–80.
Popova, E., Staraselski, Y., Brahme, A., Mishra, R., Inal, K., 2015. Coupled crystal plasticity–probabilistic cellular automata approach to model dynamic recrystallization in magnesium alloys. Int. J. Plasticity 66, 85–102.
Roberts, W., Boden, H., Ahlblom, B., 1979. Dynamic recrystallization kinetics. Metal Sci. 13, 195–205.
Rollett, A., Humphreys, F., Rohrer, G.S., Hatherly, M., 2004. Recrystallization and Related Annealing Phenomena. Elsevier.
Ryan, N., McQueen, H., 1990. Flow stress, dynamic restoration, strain hardening and ductility in hot working of 316 steel. J. Mater. Process. Technol. 21, 177–199.
Sah, J., Richardson, G., Sellars, C., 1974. Grain-size effects during dynamic recrystallization of nickel. Metal Sci. 8, 325–331.
Sakai, T., 1995. Dynamic recrystallization microstructures under hot working conditions. J. Mater. Process. Technol. 53, 349–361.
Sakai, T., Belyakov, A., Kaibyshev, R., Miura, H., Jonas, J.J., 2014. Dynamic and post-dynamic recrystallization under hot, cold and severe plastic deformation conditions. Prog. Mater. Sci. 60, 130–207.
Sakai, T., Jonas, J.J., 1984. Overview no. 35 dynamic recrystallization: mechanical and microstructural considerations. Acta Metall. 32, 189–209.
Sakai, T., Ohashi, M., 1990. Dislocation substructures developed during dynamic recrystallisation in polycrystalline nickel. Mater. Sci. Technol. 6, 1251–1257.
Sample, V., Fitzsimons, G., DeArdo, A., 1987. Dynamic softening of copper during deformation at high temperatures and strain rates. Acta Metall. 35, 367–379.

Schulson, E.M., Duval, P., et al., 2009. Creep and Fracture of Ice, vol. 1. Cambridge University Press Cambridge.
Semiatin, S., Weaver, D., Kramb, R., Fagin, P., Glavicic, M., Goetz, R., Frey, N., Antony, M., 2004. Deformation and recrystallization behavior during hot working of a coarse-grain, nickel-base superalloy ingot material. Metallurgical Mater. Trans. A 35, 679–693.
Takaki, T., Hirouchi, T., Hisakuni, Y., Yamanaka, A., Tomita, Y., 2008. Multi-phase-field model to simulate microstructure evolutions during dynamic recrystallization. Mater. Trans. 49, 2559–2565.
Takaki, T., Yoshimoto, C., Yamanaka, A., Tomita, Y., 2014. Multiscale modeling of hot-working with dynamic recrystallization by coupling microstructure evolution and macroscopic mechanical behavior. Int. J. Plasticity 52, 105–116.
Tóth, L., Jonas, J., 1992. Modelling the texture changes produced by dynamic recrystallization. Scripta Metallurgica Materialia 27, 359–363.
Vandermeer, R., Jensen, D.J., Woldt, E., 1997. Grain boundary mobility during recrystallization of copper. Metallurgical Mater. Trans. A 28, 749–754.
Viswanathan, R., Bauer, C., 1973. Kinetics of grain boundary migration in copper bicrystals with [001] rotation axes. Acta Metall. 21, 1099–1109.
Wusatowska-Sarnek, A., Miura, H., Sakai, T., 2002. Nucleation and microtexture development under dynamic recrystallization of copper. Mater. Sci. Eng. A 323, 177–186.
Zehetbauer, M., Seumer, V., 1993. Cold work hardening in stages iv and v of fcc metalsi. experiments and interpretation. Acta Metallurgica Materialia 41, 577–588.
Zhao, P., Low, T.S.E., Wang, Y., Niezgoda, S.R., 2016. An integrated full-field model of concurrent plastic deformation and microstructure evolution: application to 3d simulation of dynamic recrystallization in polycrystalline copper. Int. J. Plasticity 80, 38–55.